Dynamic behavior of active magnetic bearings-rotor system with coupling misalignment

Yazheng ZHAO*, Jin ZHOU*, Yuanke LI*, Yue ZHANG*, and Yuanping XU*
*College of Mechanical & Electrical Engineering, Nanjing University of Aeronautics and Astronautics
No. 29, Yudao Street, Nanjing, Jiangsu 210016, China
E-mail: zhj@nuaa.edu.cn

Abstract
Active magnetic bearings offer contactless support for rotor systems, making them increasingly popular in high-speed rotating machinery. However, when the rotor is connected to the motor through mechanical couplings, misalignment caused by manufacturing defects, assembly errors, or prolonged wear can introduce asymmetric excitation forces that degrade the system's dynamic performance. Existing studies often rely on idealized coupling models, fail to adequately explain experimentally observed odd–order harmonics, and lack methods for predicting the safety threshold of coupling misalignment, thereby limiting their practical value in accurately modeling rotor system dynamics and supporting engineering applications. This study investigates the dynamic behavior of an active magnetic bearings–rotor system subject to coupling misalignment. A nonlinear, time-varying stiffness model is developed by identifying harmonic components and stiffness characteristics from both simulations and experimental data. Unlike existing approaches that rely on idealized coupling assumptions, the proposed model incorporates realistic structural parameters and explains the occurrence of both even– and odd–order harmonic responses observed in practice. Based on the model, time– and frequency–domain analyses are performed under different misalignment conditions to evaluate vibration behavior and stability. Moreover, the study quantifies threshold ranges for parallel and angular misalignment under both critical and rated speeds, offering engineering guidance for safe operation. These findings offer valuable insights into the vibration mechanisms of active magnetic bearings–rotor systems with coupling misalignment and establish a foundation for condition monitoring and fault diagnosis.

Keywords : Active Magnetic Bearings, Coupling Misalignment, Nonlinear Stiffness, Critical Threshold Ranges

1. Introduction

Active Magnetic Bearings (AMBs) are increasingly used in rotor systems due to their ability to support rotors without mechanical contact, thus reducing wear and maintenance needs. In systems where the motor and rotor are connected by a coupling, power is transferred from the motor to the rotor supported by AMBs. However, misalignment between the drive shaft and the driven shaft, often resulting from manufacturing defects, assembly inaccuracies, or interface friction, can induce asymmetric forces within the AMBs-rotor system. These forces may provoke abnormal dynamic behaviors, including elevated vibrations, reduced stability, mechanical failures, and even critical safety failures under extreme operating conditions (Rangavajhala et al., 2019a and Yao et al., 2022a). Therefore, investigating the impact of coupling misalignment on the dynamic behavior of AMBs-rotor systems holds substantial theoretical and engineering significance.

Extensive research has been conducted to examine the effects of coupling misalignment on rotor. Modeling methods can be broadly categorized into two types: energy-based methods and geometric-force analysis methods. Kumar and Tiwari et al. (2021a, 2022b, and 2021b) developed a mechatronic model that integrates the misalignment effects of AMBs and protective bearings based on geometric relationships and the energy method. Ma, Tuckmantel, and other researchers (2025, 2019b, and 2024) focused on rotor systems supported by traditional mechanical bearings. Ma et al. (2025) derived the deformation of the flexible coupling and the parallel misalignment force based on the relationship between force and geometry. They observed that increasing the coupling's parallel misalignment or stiffness leads to greater vibration amplitudes and an enlarged disc-shaft gap. Under stable operating speeds, this exacerbates minor collisions and enhances fault frequency components such as 3fr and 4fr. At higher speeds, these effects result in more complex vibration

behaviors. To analyze the effects of misalignment in flexible couplings, Tuckmantel et al. (2019b) initially employed a geometric and force-based approach to model the forces and moments induced by misalignment. Subsequently, they used a finite element method to simulate variations in shaft rotation angles, capturing the cyclic behavior of these misalignment forces. Their analysis revealed distinct harmonic components arising from the misalignment. Liang et al. (2024) also derived the excitation caused by parallel misalignment based on geometric-force analysis, and concluded that coupling misalignment generates alternating meshing forces at the fundamental frequency (1×) and its harmonics (2×, 3×, 4×), resulting in significant vibration and noise. Additionally, Redmond et al. (2010) employed the energy method to model coupling misalignment in a traditional mechanical bearing-rotor system, demonstrating that coupling misalignment excites the system's 2× and 4× frequencies. The resulting alternating forces alter bearing loads and may accelerate fatigue failure.

Most existing studies have focused on misalignment modeling using energy-based and geometric-force analysis methods. However, such models still exhibit the following limitations:

(1) Existing models excessively rely on idealized representations of coupling configurations, without incorporating the actual structural parameters of typical couplings such as bellows, diaphragm, and crowned gear types. This simplification leads to inaccuracies in predicting both stiffness characteristics and harmonic components.

(2) Most current models focus on even-order harmonics (e.g., 2× and 4×) associated with misalignment, yet fail to explain the presence of odd-order harmonics (e.g., 1× and 3×) frequently observed in experimental data. These odd harmonics, induced by coupling misalignment, are physically plausible and experimentally verifiable.

(3) Existing approaches provide only qualitative insights into how misalignment affects vibration amplitude and frequency, without establishing quantitative dynamic models capable of defining safety thresholds for misalignment under critical speeds and rated operating conditions. This limitation severely restricts their practical utility in ensuring the reliable operation of rotor systems.

To address these gaps, this study develops an AMBs-rotor model with coupling misalignment. A time-varying nonlinear stiffness model is constructed by identifying coupling stiffness and harmonic terms from simulation and experiments, offering physical interpretability beyond idealized assumptions. Based on this model, the time- and frequency-domain response characteristics under different misalignment cases, along with the critical threshold ranges at both the critical and rated speeds, are analyzed.

2. Modelling

2.1 Coupling modelling

As shown in Fig. 1, the AMBs-rotor system is composed of a motor, a coupling, a rotor, and two magnetic bearings. The coupling is used to connect the motor shaft and the rotor shaft.

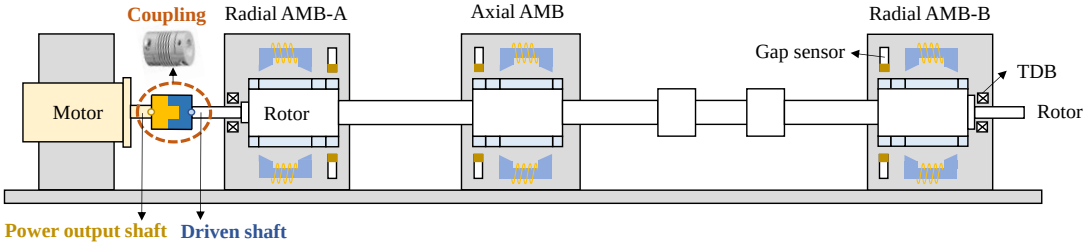

Fig. 1 Schematic diagram of an AMBs-rotor system.

Manufacturing errors, assembly mistakes, and operational deformations can cause misalignment, including parallel (δ), angular (ϑ), or combined misalignment (δ and ϑ), as shown in Fig. 2. This misalignment introduces periodic loads that impact the rotor's dynamic behavior.

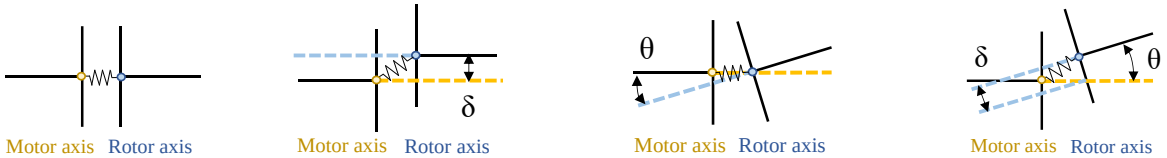

(a) Ideal status (b) Parallel misalignment δ (c) Angular misalignment ϑ (d) Combined misalignment δ, ϑ

Fig. 2 Schematic diagram of ideal and misaligned states of the coupling.

The coupling is modeled as a massless elastic element that can transmit both translational and rotational loads, with equivalent stiffnesses in the x, y, θ_x, and θ_y directions denoted as k_x, k_y, k_{θ_x} and k_{θ_y}, respectively. Let$(x_m, y_m, \theta_{xm}, \theta_{ym})$ and $(x_r, y_r, \theta_{xr}, \theta_{yr})$ represent the generalized coordinates at the motor-coupling and coupling-rotor junctions. The relative displacements between the motor and rotor sides of the coupling are defined as:

$$\begin{cases} \Delta x = (x_r - x_m) + \delta\cos(\omega t + \varphi_\delta) \\ \Delta y = (y_r - y_m) + \delta\sin(\omega t + \varphi_\delta) \\ \Delta\theta_x = \left(\theta_{x_r} - \theta_{x_m}\right) + \vartheta\cos(\omega t + \varphi_\vartheta) \\ \Delta\theta_y = \left(\theta_{y_r} - \theta_{y_m}\right) + \vartheta\sin(\omega t + \varphi_\vartheta) \end{cases} \tag{1}$$

where ω is the rotational speed, t is time, and φ_δ and φ_ϑ represent the phase angles of the parallel and angular misalignments, respectively. The deformation energy of the coupling can thus be written as:

$$V_c = \frac{1}{2}k_x\Delta x^2 + \frac{1}{2}k_y\Delta y^2 + \frac{1}{2}k_{\theta_x}\Delta\theta_x^2 + \frac{1}{2}k_{\theta_y}\Delta\theta_y^2 \tag{2}$$

To account for the periodic variation in coupling stiffness caused by structural asymmetry, assembly errors, and material fatigue, the coupling stiffness is assumed to vary periodically with the rotor's rotational frequency and its harmonics. Using a truncated Fourier series, the time-varying stiffnesses are modeled as:

$$\begin{cases} k_x = k_{x_0}[1 + \sum_{n=1}^{N} a_n \cos(n\omega t)] \\ k_y = k_{y_0}[1 + \sum_{n=1}^{N} b_n \cos(n\omega t)] \\ k_{\theta_x} = k_{\theta_{x_0}}[1 + \sum_{n=1}^{N} c_n \cos(n\omega t)] \\ k_{\theta_y} = k_{\theta_{y_0}}[1 + \sum_{n=1}^{N} d_n \cos(n\omega t)] \end{cases} \tag{3}$$

where $(k_{x_0}, k_{x_0}, k_{\theta_{x_0}}, k_{\theta_{y_0}})$ represent the average stiffness of the coupling in the translational and rotational directions, reflecting its static characteristics. (a_n, b_n, c_n, d_n) are the harmonic coefficients in the translational and rotational directions. N is the order of harmonic. By substituting the Eqs. (1) and (2) into the deformation energy, the coupling's potential energy V_c is obtained. Given that the coupling is assumed to be massless, its Lagrangian reduces to $L = -V_c$. Applying the Lagrange equations then yields the misalignment-induced generalized force vector $\boldsymbol{Q_M} = \{F_{x_r}, F_{y_r}, F_{\theta_{y_r}}, F_{\theta_{y_r}}\}$ acting on the rotor side:

$$\begin{cases} F_{x_r} = k_{x_0}[1 + \sum_{n=1}^{N} a_n \cos(n\omega t)][(x_r - x_m) + \delta\cos(\omega t + \varphi_\delta)] \\ F_{y_r} = k_{y_0}[1 + \sum_{n=1}^{N} b_n \cos(n\omega t)][(y_r - y_m) + \delta\sin(\omega t + \varphi_\delta)] \\ F_{\theta_{x_r}} = k_{\theta_{x_0}}[1 + \sum_{n=1}^{N} c_n \cos(n\omega t)]\left[\left(\theta_{x_r} - \theta_{x_m}\right) + \vartheta\cos(\omega t + \varphi_\vartheta)\right] \\ F_{\theta_{y_r}} = k_{\theta_{y_0}}[1 + \sum_{n=1}^{N} d_n \cos(n\omega t)]\left[\left(\theta_{y_r} - \theta_{y_m}\right) + \vartheta\sin(\omega t + \varphi_\vartheta)\right] \end{cases} \tag{4}$$

2.2 Electromechanical model of the AMB-rotor system with coupling

The dynamic model of the AMB-rotor system with coupling misalignment is expressed as:

$$\boldsymbol{M}\ddot{\boldsymbol{q}}(t) + (\boldsymbol{C} + \Omega\boldsymbol{G})\dot{\boldsymbol{q}}(t) + \boldsymbol{K}\boldsymbol{q}(t) = \boldsymbol{T}_{\boldsymbol{M}}^{\mathrm{T}}\boldsymbol{Q}_{\boldsymbol{M}}(t) + \boldsymbol{T}_{\boldsymbol{A}}^{\mathrm{T}}\boldsymbol{F}_{\boldsymbol{A}}(t) + \boldsymbol{T}_{\boldsymbol{U}}^{\mathrm{T}}\boldsymbol{F}_{\boldsymbol{U}}(t) \tag{5}$$

where $\boldsymbol{M}$, $\boldsymbol{C}$, $\boldsymbol{G}$, $\boldsymbol{K}$ are the mass, damping, gyroscopic, and stiffness matrices of the rotor and $\boldsymbol{q}$ represents the generalized coordinates of the rotor. $\boldsymbol{T_M}$, $\boldsymbol{T_A}$, and $\boldsymbol{T_U}$ are transformation matrices for coupling misalignment force $\boldsymbol{Q_M}$, magnetic bearing force $\boldsymbol{F_A}$, and unbalance force $\boldsymbol{F_U}$, respectively. The unbalance force is modeled as:

$$\boldsymbol{F_U} = mr \cdot e^{j\varphi_u} \tag{6}$$

where m is the unbalance mass, r is eccentricity, and φ_u is the initial phase of the unbalance.

The electromagnetic force from the AMBs is linearized as:

$$\boldsymbol{F}_A = -k_s\boldsymbol{q_s} + k_i\boldsymbol{i_a} \tag{7}$$

where k_s and k_i are the displacement and current stiffnesses, and $\boldsymbol{q_s}$ is the translational displacement vector at the AMB actuator locations, and the control current $\boldsymbol{i_a}$ is derived from a closed-loop system that includes the sensor, controller, and amplifier models.

$$\boldsymbol{i_a} = \frac{i_a}{u_c}\frac{u_c}{u_e}(\boldsymbol{u_r} - \boldsymbol{u_s}) = G_a(s)G_c(s)[\boldsymbol{u_r} - G_s(s)\boldsymbol{q_s}] \tag{8}$$

where $G_s(s)$, $G_a(s)$, and $G_c(s)$ denote the transfer functions of the displacement sensor, power amplifier, and controller, respectively, and are given by:

$$\begin{cases} G_s(s) = k_s \\ G_a(s) = k_a \frac{1}{T_a s+1} \frac{1}{T_b s+1} \\ G_c(s) = K_P + \frac{K_I}{s} + \frac{K_D s}{T_D s+1} \end{cases} \tag{9}$$

where k_s is the sensor gain, k_a is the static gain of the power amplifier, T_a and T_b are the time constants of the power amplifier, K_P, K_I, and K_D are the proportional, integral, and derivative gains of the controller, respectively, and T_D is the time constant of the derivative filter. By introducing the state-space vector $\{\dot{q} \;\; q\}^{\mathrm{T}}$, the differential equation of motion Eq. (6) is transformed into the state-space form, expressed as:

$$\begin{Bmatrix} \ddot{q} \\ \dot{q} \end{Bmatrix} = \begin{bmatrix} \mathbf{0} & \boldsymbol{I} \\ -\boldsymbol{M}^{-1}(\boldsymbol{K} - k_s \boldsymbol{T_A}^{\mathrm{T}} \boldsymbol{T_A}) & -\boldsymbol{M}^{-1}(\boldsymbol{C} + \Omega \boldsymbol{G}) \end{bmatrix} \begin{Bmatrix} \dot{q} \\ q \end{Bmatrix} + \begin{bmatrix} \mathbf{0} \\ \boldsymbol{M}^{-1} \boldsymbol{T_M}^{\mathrm{T}} \end{bmatrix} \boldsymbol{Q_M} + \begin{bmatrix} \mathbf{0} \\ k_i \boldsymbol{M}^{-1} \boldsymbol{T_A}^{\mathrm{T}} \end{bmatrix} \boldsymbol{i_a} + \begin{bmatrix} \mathbf{0} \\ \boldsymbol{M}^{-1} \boldsymbol{T_U}^{\mathrm{T}} \end{bmatrix} \boldsymbol{F_u} \tag{10}$$

3. Parameter Identification of Coupling

The static stiffness and harmonic coefficients in Eq. (5) are affected by factors like coupling type, manufacturing tolerance, and preload, making them hard to determine accurately.

3.1 Static Stiffness

Static stiffness reflects the average stiffness of the coupling in translation and rotation. To obtain these values, finite element simulations are performed by applying force and torque to one side of the coupling and measuring the displacements. Figs. 3 and 4 show the boundary conditions and deformation results used in the simulations.

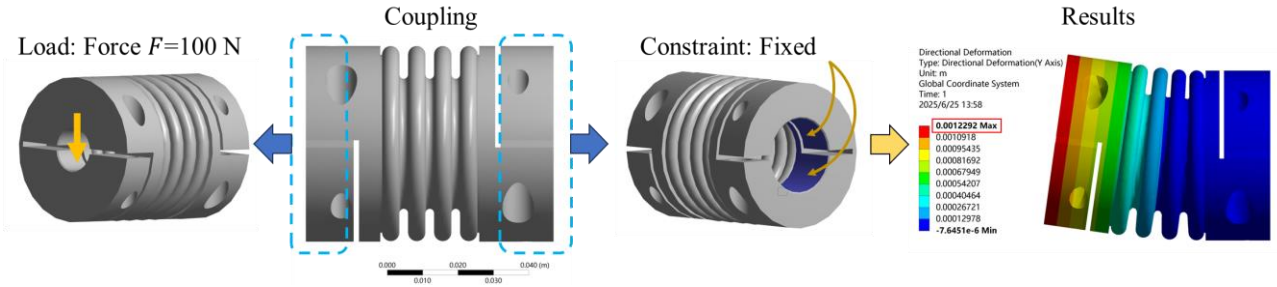

Fig. 3 Load, constraints, and deformation results for calculating translational stiffness

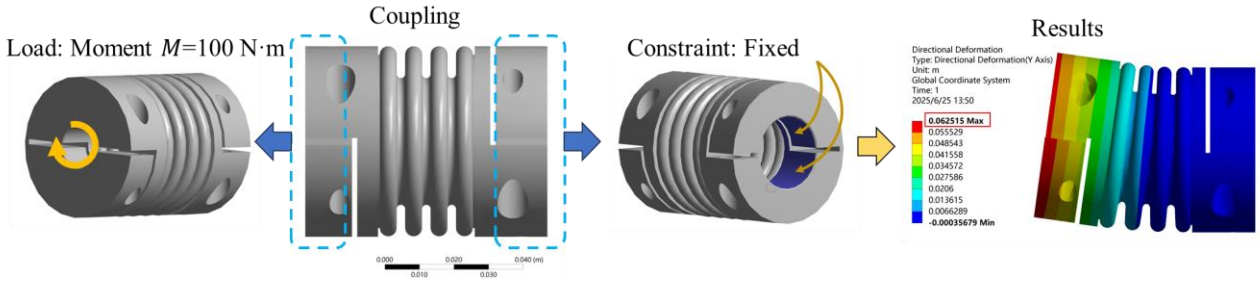

Fig. 4 Load, constraints, and deformation results for calculating rotational stiffness

The static stiffness values can be calculated based on the linear relationships between force F and displacement Δ, and between moment M and angular displacement $\Delta\theta$:

$$\begin{cases} k_{x_0} = k_{y_0} = \frac{F}{\Delta} = \frac{100\mathrm{N}}{0.0012292\mathrm{m}} = 8.14 \times 10^4 \mathrm{N/m} \\ k_{\theta_{x_0}} = k_{\theta_{y_0}} = \frac{M}{\Delta\theta} = \frac{100\mathrm{N \cdot m}}{arctan(0.062515\mathrm{m}/0.072\mathrm{m})} = 139.74\mathrm{N \cdot m/rad} \end{cases} \tag{11}$$

3.2 Harmonic Coefficients

Since harmonic components in coupling stiffness are hard to obtain directly through simulations or analytical methods, this study uses FFT to extract the amplitudes of the main and harmonic frequencies from experimental time-domain data. These results are then compared with simulation outputs to identify the harmonic coefficients.

The time-domain displacement response is $y(t)$, with a sampling frequency of f_s. Data of length $N = f_s \cdot 1$ is

extracted from the time interval $[t_i, t_i + 1]$ at the i-th second, and FFT is applied:

$$X(f) = FFT\{y(t)\}, f = 0{:}\frac{1}{t}{:}f_{max} \tag{12}$$

To eliminate the DC component, let $X(0)$=0. Then, the maximum amplitude of path 1 is extracted near the fundamental frequency and each higher-order harmonic frequency, denoted as:

$$NF_{i,1}^{exp} = max\{|X(f)||f_i - 5 \le f \le f_i + 5\}, i = 1, 2, \dots\dots, M \tag{13}$$

where f_i denotes the frequency of the i-th order, and M represents the number of harmonic orders. By summing the amplitudes of the fundamental and higher-order harmonic frequencies across the four channels, the overall experimental response amplitude of the system is obtained, respectively.

$$NF_i^{exp} = \sum_{j=1}^{4} NF_{i,j}^{exp}, i = 1, 2, \dots\dots, M \tag{14}$$

To identify the harmonic coefficients from the experimental data, the Particle Swarm Optimization (PSO) algorithm is employed to search and optimize the parameter vector $\mathbf{p} = \{a_n, b_n, c_n, d_n | n = 1, 2, \dots\dots, N\}$. The objective function is defined to minimize the error between the simulated and experimental amplitude values in the frequency domain:

$$\min_{\mathbf{p}} J(\mathbf{p}) = \sum_{i=1}^{M} \left| \mathrm{NF}_i^{\mathrm{sim}}(\mathbf{p}) - \mathrm{NF}_i^{\mathrm{exp}} \right| \quad \text{s.t. } 0 \le \mathbf{p} \le 1 \tag{15}$$

where $\mathrm{NF}_i^{\mathrm{sim}}$ denotes the simulated frequency-domain amplitude under the given parameter vector $\mathbf{p}$. Optimization is performed based on an error feedback mechanism between the simulation and experimental results. The PSO algorithm parameters are set with a population size of 50 and a maximum of 100 iterations.

4. Numerical simulation results

4.1 Time-domain and frequency-domain responses under different misalignment conditions

Numerical simulations are conducted under four conditions, as shown in Figs. 5-8. In Case 1, with only unbalance present, a clear fundamental frequency (1X) peak is observed without higher-order harmonics. In Case 2, parallel misalignment causes periodic waveform modulation, significantly increasing 1X, and higher-order harmonics (2X, 3X). In Case 3, 1X increases noticeably, with weak 2X and 3X components. In Case 4, combined misalignment leads to a marked increase in 1X, 2X, and 3X amplitudes. Thus, both parallel and angular misalignments induce significant higher-order harmonics and amplify the fundamental vibration, with parallel misalignment having a greater impact in this system. Although 2X is commonly seen as the key indicator of misalignment, it is important to note that coupling misalignment also increases 1X amplitude and excites additional higher-order harmonics.

Case 1: No misalignment, unbalance present (me = 1.25×10^{-4}kg·m)

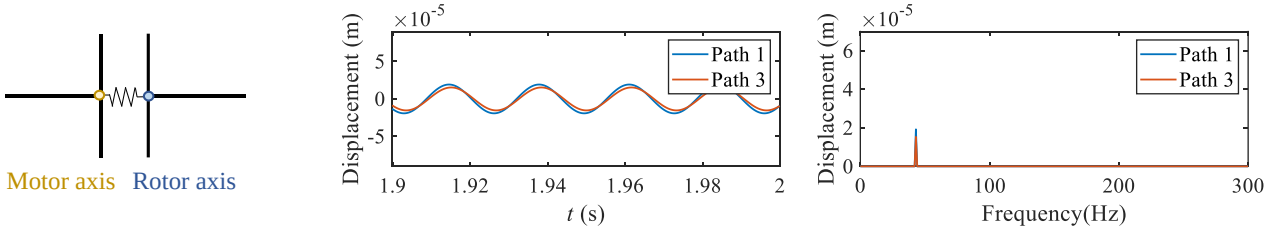

(a) (b) (c)

Fig. 5 Simulation results of Case 1 at a rotation speed of 4000 rpm: (a) Location schematic diagram of motor axis and rotor axis (b) Time-domain response (c) Frequency-domain response.

Case 2: Parallel misalignment present (δ = 5×10^{-4}m), no angular misalignment, unbalance present (me = 1.25×10^{-4}kg·m)

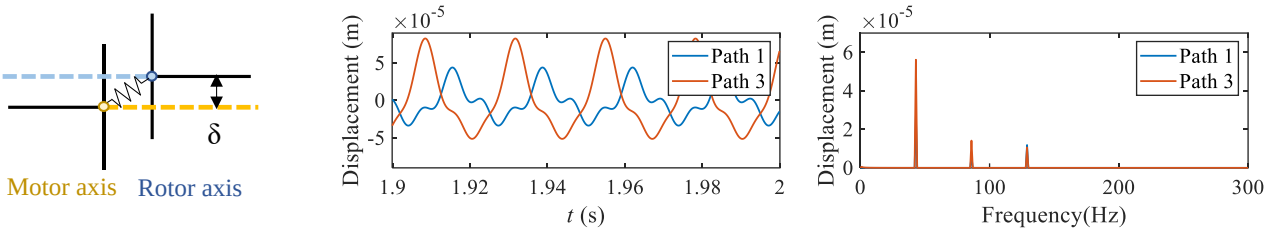

(a) (b) (c)

Fig. 6 Simulation results of Case 2 at a rotation speed of 4000 rpm: (a) Location schematic diagram of motor axis and rotor axis (b) Time-domain response (c) Frequency-domain response.

Case 3: No parallel misalignment, angular misalignment present ($\vartheta = 1°$), unbalance present ($me = 1.25\times10^{-4}$kg·m)

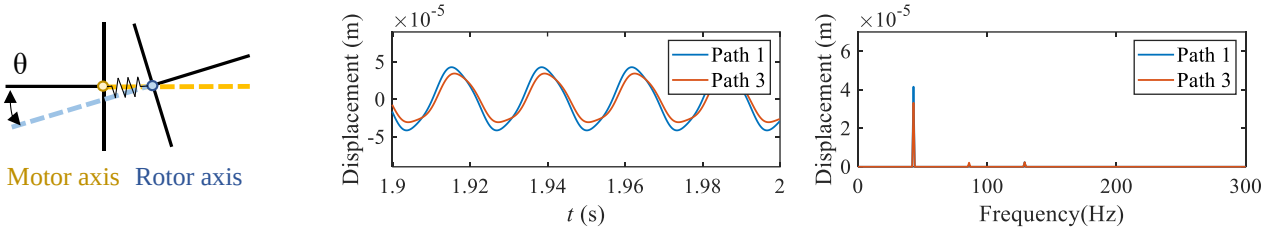

(a) (b) (c)

Fig. 7 Simulation results of Case 3 at a rotation speed of 4000 rpm: (a) Location schematic diagram of motor axis and rotor axis (b) Time-domain response (c) Frequency-domain response.

Case 4: Parallel and angular misalignment present ($\delta = 5\times10^{-4}$m, $\vartheta = 1°$), unbalance present (me=1.25×10^{-4}kg·m)

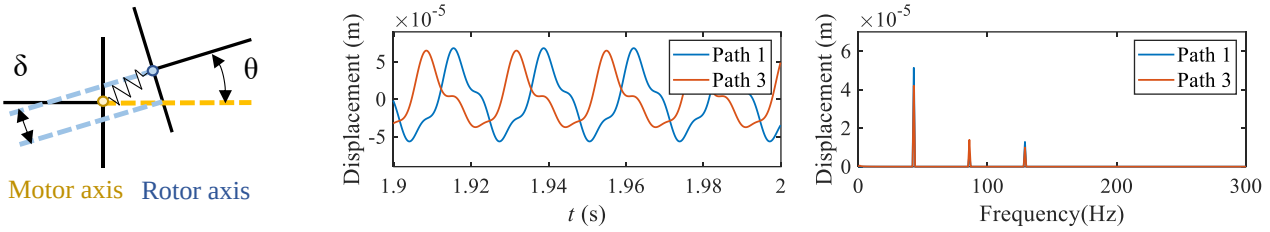

(a) (b) (c)

Fig. 8 Simulation results of Case 4 at a rotation speed of 4000 rpm: (a) Location schematic diagram of motor axis and rotor axis (b) Time-domain response (c) Frequency-domain response.

4.2 Critical Misalignment Threshold

Fig. 9 shows the displacement responses of Path 1 to Path 4 during the speed-up process. It can be seen that 2580 rpm (near the first rigid-body mode frequency) and 4000 rpm (rated speed) are two critical speeds that require particular attention in the threshold analysis.

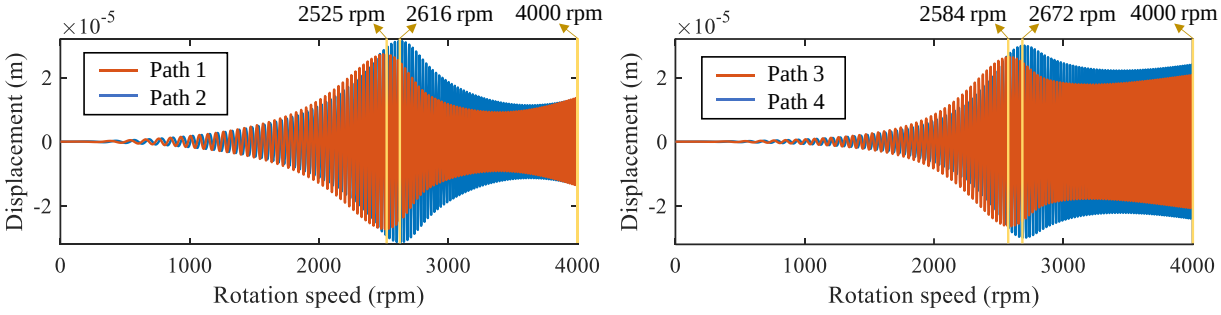

Fig. 9 runup response under Case 1.

The international standard ISO 7919-1 specifies zone limit criteria as shown in Table 1, where Zones A, B, C, and D

represent four different levels of displacement requirements. Zone A is normal for new machines; Zone B is safe for long-term use; Zone C allows only short-term operation until repairs; Zone D indicates severe vibration that can damage the machine.

Table 1 Zone limit criteria

Zone limit	Boundary value (C_{min}= Minimum radial clearance between the rotor and the stator)	Limit value in this study (C_{min}=125 μm)
A/B zone boundary	0.3 C_{min}	37.5 μm
B/C zone boundary	0.4 C_{min}	50.0 μm
C/D zone boundary	0.5 C_{min}	62.5 μm

Figure 10 shows contour plots of the maximum peak displacement at two critical speeds under parallel and angular misalignment, along with the displacement zones defined by the Zone Limits in Table 1, providing a reference for AMBs-rotor system stability assessment.

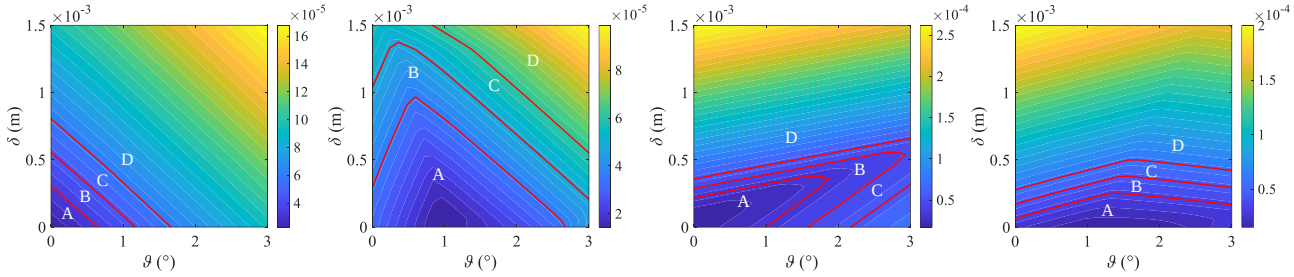

(a) Path 1 (b) Path 2 (c) Path 3 (d) Path 4

Fig. 10 Contour plot of the maximum peak displacement at a rotational speed of 2580 rpm.

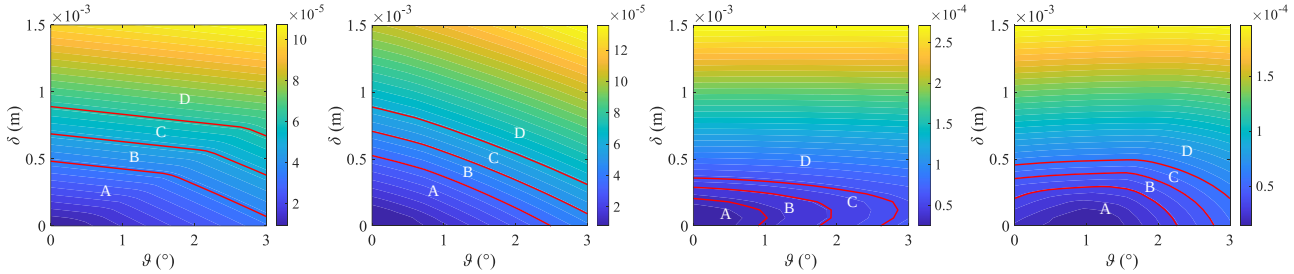

(a) Path 1 (b) Path 2 (c) Path 3 (d) Path 4

Fig. 11 Contour plot of the maximum peak displacement at a rotational speed of 4000 rpm.

Fig. 12 shows the threshold ranges of parallel and angular misalignment parameters at two critical speeds. Different paths show clear differences in misalignment tolerance at 2580 rpm and 4000 rpm. As speed increases, the threshold ranges change, showing that speed affects misalignment sensitivity. Also, vibration displacement is generally required to stay within Zone B. The blue areas in the figure indicate the allowable misalignment at the two key speeds.

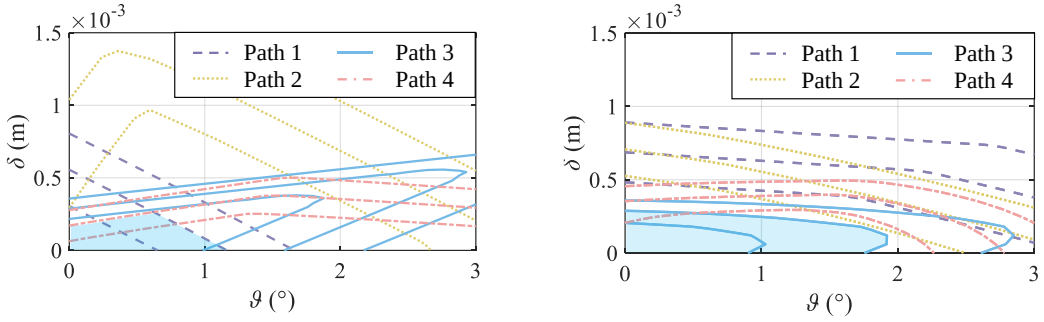

(a) Rotation speed of 2580 rpm (b) Rotation speed of 4000 rpm

Fig.12 Threshold range of parallel and angular misalignment parameters.

5. Conclusions

In this work, the dynamic behavior of an AMBs-rotor system with coupling misalignment is analyzed. The main conclusions are as follows:

(1) An AMBs-rotor model incorporating coupling misalignment is developed. The model captures the nonlinear and time-varying stiffness characteristics of the coupling caused by both parallel and angular misalignments. Key uncertain parameters within the nonlinear stiffness, specifically static stiffness and harmonic coefficients, are identified through mechanical simulation and frequency-domain experimental analysis.

(2) Numerical simulations are conducted to analyze the system's vibration characteristics under various conditions. The key finding is that both parallel and angular misalignments significantly amplify the fundamental frequency (1X) and higher-order harmonics (2X, 3X), with parallel misalignment exerting a stronger influence. While 2X is often considered the primary indicator of misalignment, coupling misalignment also notably increases the 1X amplitude and excites additional higher-order harmonics.

(3) The misalignment threshold of the active magnetic bearing–rotor system is critically evaluated at two key speeds: 2580 rpm (near the first rigid-body mode frequency) and 4000 rpm (rated speed). Based on the displacement zone criteria specified in ISO 7919-1, significant differences in misalignment tolerance emerge across different speeds and measurement paths, and the system's sensitivity to misalignment changes as rotational speed increases. To ensure system stability and long-term safe operation, vibration displacement should be maintained within the analyzed threshold ranges. This provides an important reference for misalignment control and stability assessment of the active magnetic bearing–rotor system.

Acknowledgments and conflicts of interest

This work was supported by the National Natural Science Foundation of China (Grant No. 52475060), the State Key Laboratory of Mechanics and Control for Aerospace Structures (Grant No. MCAS-S-0425G02), and the Outstanding Doctoral Dissertation Funding of NUAA (Grant No. BCXJ25-13).

The authors declare that they have no known competing financial interests or personal relationships that could have appeared to influence the work reported in this paper.

References

Kumar, P. and Tiwari, R., Finite element modelling, analysis and identification using novel trial misalignment approach in an unbalanced and misaligned flexible rotor system levitated by active magnetic bearings, Mechanical Systems and Signal Processing, Vol.152 (2021), pp.107454.

Kumar, P. and Tiwari, R., Dynamic analysis and identification of unbalance and misalignment in a rigid rotor with two offset discs levitated by active magnetic bearings: a novel trial misalignment approach, Propulsion and Power Research, Vol.10, No.1 (2021), pp.58–82.

Liang, Z., Cai, W., Zhou, Y. and others, An analysis of abnormal vibration and noise caused by shaft coupling misalignment of high-speed train, Engineering Failure Analysis, Vol.165 (2024), pp.108789.

Ma, X., Li, Z., Xiang, J. and others, Vibration characteristics of rotor system with coupling misalignment and disc-shaft nonlinear contact, Mechanical Systems and Signal Processing, Vol.223 (2025), pp.111839.

Redmond, I., Study of a misaligned flexibly coupled shaft system having nonlinear bearings and cyclic coupling stiffness—theoretical model and analysis, Journal of Sound and Vibration, Vol.329, No.6 (2010), pp.700–720.

Rangavajhala, S.S., Tiwari, R. and Kannababu, C., Model-based analysis and identification of multiple fault parameters in coupled rotor systems with offset discs in the presence of angular misalignment and integrated with an active magnetic bearing, Journal of Sound and Vibration, Vol.450 (2019), pp.109–140.

Tiwari, R. and Kumar, P., An innovative virtual trial misalignment approach for identification of unbalance, sensor and active magnetic bearing misalignment along with its stiffness parameters in a magnetically levitated flexible rotor system, Mechanical Systems and Signal Processing, Vol.167 (2022), pp.108540.

Tuckmantel, F.W.S. and Cavalca, K.L., Vibration signatures of a rotor-coupling-bearing system under angular misalignment, Mechanism and Machine Theory, Vol.133 (2019), pp.559–583.

Yao, R., Zhou, J., Guan, X. and others, Dynamic characteristics of magnetic bearing system with coupling misalignment, Journal of Vibration, Measurement and Diagnosis, Vol.42, No.1 (2022), pp.124–128.